CrossMark

Rapidly Estimated Seismic Source Parameters for the 16 September 2015 Illapel, Chile M_w 8.3 Earthquake

LINGLING YE,[1] THORNE LAY,[2] HIROO KANAMORI,[1] and KEITH D. KOPER[3]

Abstract—On 16 September 2015, a great (M_w 8.3) interplate thrust earthquake ruptured offshore Illapel, Chile, producing a 4.7-m local tsunami. The last major rupture in the region was a 1943 M_S 7.9 event. Seismic methods for rapidly characterizing the source process, of value for tsunami warning, were applied. The source moment tensor could be obtained robustly by W-phase inversion both within minutes (Chilean researchers had a good solution using regional data within 5 min) and within an hour using broadband seismic data. Short-period teleseismic P wave back-projections indicate northward rupture expansion from the hypocenter at a modest rupture expansion velocity of 1.5–2.0 km/s. Finite-fault inversions of teleseismic P and SH waves using that range of rupture velocities and a range of dips from 16°, consistent with the local slab geometry and some moment tensor solutions, to 22°, consistent with long-period moment tensor inversions, indicate a 180- to 240-km bilateral along-strike rupture zone with larger slip northwest to north of the epicenter (with peak slip of 7–10 m). Using a shallower fault model dip shifts slip seaward toward the trench, while a steeper dip moves it closer to the coastline. Slip separates into two patches as assumed rupture velocity increases. In all cases, localized ∼5 m slip extends down-dip below the coast north of the epicenter. The seismic moment estimates for the range of faulting parameters considered vary from 3.7×10^{21} Nm (dip 16°) to 2.7×10^{21} Nm (dip 22°), the static stress drop estimates range from 2.6 to 3.5 MPa, and the radiated seismic energy, up to 1 Hz, is about 2.2–3.15×10^{16} J.

Key words: 2015 Illapel earthquake, Chilean seismic gaps, rupture process, seismic rupture parameters.

[1] Seismological Laboratory, California Institute of Technology, MS 252-21, Pasadena, CA 91101, USA.
[2] Department of Earth and Planetary Sciences, University of California Santa Cruz, Santa Cruz, CA 95064, USA. E-mail: tlay@ucsc.edu
[3] Department of Geology and Geophysics, University of Utah, Salt Lake City, UT 84112, USA.

1. Introduction

The subduction zone along Chile was struck by the third great earthquake in 6 years when the plate boundary offshore of Illapel ruptured from 30.25°S to 32.5°S in an M_W 8.3 event on 16 September 2015 (31.570°S, 71.670°W, 22:54:33 UTC (USGS National Earthquake Information Center—NEIC: http://earthquake.usgs.gov/earthquakes/) (Fig. 1). This region had been identified as a seismic gap based on the occurrence of prior large earthquakes in 1943, 1880, and 1730 (KELLEHER 1972; NISHENKO 1985; BECK *et al*. 1998). The region just to the south (32°S to 34.5°S) ruptured most recently in the 9 July 1971 [M_S 7.9, M_W 7.8, (ISC-GEM)] and 3 March 1985 [M_S 7.8, M_W 7.9 (CMT)] Valparaíso earthquakes as well as previously in the great 17 August 1906 (M_S 8.4) earthquake (e.g., COMTE *et al*. 1986; CHRISTENSEN and RUFF 1986). The region to the north (26°S to 30.25°S) ruptured in the great 11 November 1922 M_S 8.3 earthquake (e.g., BECK *et al*. 1998) (actual rupture is likely to be offshore, as large tsunami was produced, so the ISC-GEM location in Fig. 1a is too far inland). The 1922 rupture zone has been seismically relatively quiet since then.

The rapid global Centroid-Moment Tensor (gCMT) solution for this event (http://www.globalcmt.org/CMTsearch.html) indicates an almost pure double-couple faulting geometry with strike, $\phi = 5°$, dip, $\delta = 22°$, and rake, $\lambda = 106°$, at a centroid depth $h_c = 17.8$ km with a centroid location northwest of the hypocenter (31.22°S, 72.27°W) (Fig. 1). The centroid time shift t_c is 47.9 s and seismic moment M_0 is 2.86×10^{21} Nm (M_w 8.2). The W-phase solution from CNRS has $M_0 = 2.68 \times 10^{21}$ Nm, with a centroid location at 31.02°S and 72.04°W
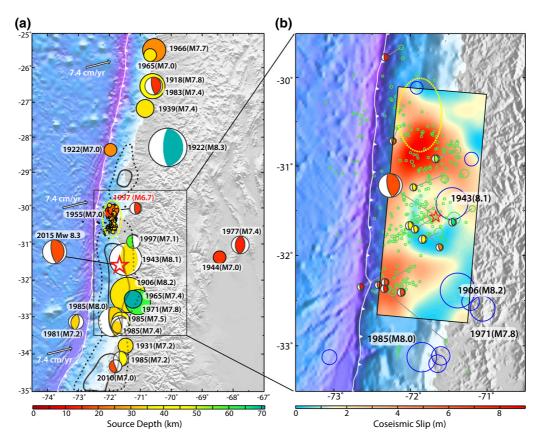
Figure 1
Maps of seismicity in the source region of the 16 September 2015 Illapel, Chile earthquake with the *inset* (**b**) showing a slip distribution inverted from teleseismic body waves. The USGS-NEIC epicenter is indicated by the *red star*. The global centroid moment tensor (gCMT) mechanism is shown with a *line* to the epicenter in *both panels* and plotted at the gCMT centroid in (**b**). gCMT solutions for other large events are shown at their respective centroid locations, color-coded by depth and scaled proportional to their moments. Mechanisms for the great 1943 and 1922 events are from BECK *et al.* ([1998](#)). Preceding earthquakes larger than magnitude 7.0 from 1900 to 2015 from the ISC-GEM catalog are shown by the *depth-colored circles* in (**a**) and the *blue circles* in (**b**) (or focal mechanisms, if known) with each radius scaled by estimated magnitude (year and magnitude are indicated). The seismicity of the 1997 Coquimbo swarm is outlined in *yellow*. The *black contours* in (**a**) are the fault locking model of MÉTOIS *et al.* ([2012](#)) for south of −28°, with the *dashed curve* indicating 50 % locking and the *solid curve* 90 % locking. The *small green circles* in (**b**) are USGS-NEIC epicenters of aftershocks in the first 2 weeks following the 2015 mainshock. The *rectangular area* in (**b**) is the slip distribution estimated by teleseismic P and SH inversion for $V_r = 2.0$ km/s and dip 22° in this study (Fig. [4](#)d). The *toothed white curves* indicate the trench position

with $h_c = 17.5$ km, and best-double-couple $\phi = 2.7°$, $\delta = 22.3°$, and $\lambda = 94.3°$ (http://wphase. unistra.fr/events/illapel_2015/index.html). The USGS-NEIC W-phase solution has slightly larger $M_0 = 3.19 \times 10^{21}$ Nm (M_W 8.3) and $h_c = 25.5$ km, with a best-double-couple geometry of $\phi = 353°$, $\delta = 19°$ and $\lambda = 83°$. Although the precise seismic moment, dip and source depth vary among these early point-source estimates due to intrinsic trade-offs and limitations of long-period determinations, the

location and size estimates confirm the potential for large tsunami generation.

The Nazca plate has been underthrusting South America near the 2015 rupture at about 74 mm/year (DEMETS *et al.* 2010) for the 72 years since the 6 April 1943 rupture, suggesting that up to 5.3 m of slip deficit may have accumulated since then. Accumulation of slip deficit on the Chilean megathrust has been measured using the progressively eastward deflection of GPS stations in Chile for almost two

decades (e.g., NORABUENA *et al.* 1998; KENDRICK *et al.* 1999). Several early interpretations modeled GPS observations with a uniformly totally locked shallow plate boundary and a significantly deforming back-arc region (e.g., KENDRICK *et al.* 2001; KHAZARADZE and KLOTZ 2003; BROOKS 2003). VIGNY *et al.* (2009) conclude that only 40–45 % of the total convergence rate between the Nazca and South American plates is causing accumulation of elastic deformation in the upper plate. Recent interpretations indicate that the plate boundary slip deficit is a large fraction of the plate convergence near 31°S, but reduces along 31.5–32°S (MORENO *et al.* 2010). MÉTOIS *et al.* (2012) also argue for variable coupling along the plate boundary (Fig. 1a), but find nearly 100 % coupling from 31°S to 33°S at depths from 15 to 45 km on the megathrust, corresponding to the 2015 rupture area in Fig. 1b. Weak coupling from 30°S to 31°S is indicated for the region to the north of the rupture where the July 1997 Coquimbo swarm (Fig. 1) occurred (e.g., GARDI *et al.* 2006; HOLTKAMP *et al.* 2011; BRODSKY and LAY 2014).

Recent studies of large subduction-zone earthquakes clearly demonstrated that although the long-term strain accumulation patterns can be mapped quantitatively with GPS, the occurrence of individual earthquakes exhibit significant complexity in both spatial and temporal distributions, especially along subduction zones where events with variable rupture length have occurred. Given this complexity, when a large earthquake has occurred, very rapid assessment of the event is critically important for early hazard warning of aftershocks and tsunamis, immediate post-earthquake emergency efforts, and assessment of regional seismic potential immediately following the event. With the currently available real-time data and analysis methods, we can assess the first-order tsunami potential in 5–20 min using long-period seismic waves and high-rate GPS, and characterize the slip distribution and the spectral characteristics of the source within a few hours. In view of this importance, we report here the primary source parameters estimated from rapid seismological methods for the 16 September 2015 event and discuss the rupture in the context of the historic earthquake activity and the plate locking determinations. We examine point-source parameters and tectonic setting to constrain the faulting geometry, back-projection of teleseismic P waves to constrain the rupture dimensions and expansion velocity, and then perform finite-fault inversions for which we estimate source parameters for the event.

2. Rapid Seismic Analysis of the 2015 M_w 8.3 Earthquake

2.1. Point-Source Solutions

For tsunami warning purposes, it is desirable to estimate the earthquake mechanism, seismic moment, and depth within a few minutes. We applied the W-phase inversion method (KANAMORI and RIVERA 2008; DUPUTEL *et al.* 2012) to regional three-component ground displacements in the passband 1–5 mHz from 10 to 11 global seismic stations (22 components) within 10° of the epicenter. For source depths of 17.5–25.5 km this analysis yielded shallow-dipping (13.7°–17.4°) thrust mechanisms with moments of 3.5–3.4 × 10^{21} Nm, and could be completed within five to ten minutes if operated in real time, as it requires only 200–300 s of recorded signal after the origin time. Centroid time shifts, t_c, of 42–41 s were found, which are only moderately longer than the value of 36 s predicted based on the average relationship found by Duputel et al. (2013) of $t_c = 2.59 \times 10^{-6} M_0^{1/3}$ (for M_0 in Nm). This provides a rapid determination that the source was not a tsunami earthquake, as such events have significantly larger t_c shifts relative to the average (DUPUTEL *et al.* 2013), even while the seismic moment, mechanism, and location of the 2015 event do suggest significant tsunamigenesis.

An operational application of regional W-phase inversion was performed by the Chilean National Seismological Center of the University of Chile, and provided a solution within 5 min using data from 22 stations within 12° of the epicenter, with M_W 8.1. This information was automatically transmitted to the Navy Hydrographic Service in charge of the tsunami alerts, and the Emergency Office of the Interior deployed an evacuation plan for the coastal population. It is estimated that about 1 million people were

evacuated from various exposed regions in central Chile.

Point-source inversions using global data for the 16 September 2015 Illapel mainshock reported by routine rapid seismic wave processing have moderately varying thrust plane dip, centroid depth, and seismic moment. For shallow thrust events the product $M_0 \times \sin(2\delta)$ is well determined by long-period inversions. However, there is strong trade-off between dip and seismic moment, such that the estimated moment is about 30 % larger for a 16° dip than for a 22° dip. We performed W-phase inversions using varying global data distributions finding centroid depths of 25.5–30.5 km and dips of 16.1° to 18.5° with centroid locations being dependent on the data set.

To provide an independent estimate of the dip to stabilize the trade-off between dip and moment, we examined the slab geometry models of HAYES and WALD (2009) and HAYES et al. (2012) which indicate a relatively planar plate boundary interface dipping at ~16.5° near 31°S. Relative to the trench position, the USGS-NEIC hypocenter is compatible with a dip of ~16° as well. Thus, there is a range of dip estimates of from about 16° to 22° quickly available, with the steeper dip requiring some reduction of dip at shallow depth on the megathrust to connect to the trench. There is no clear resolution of shallow curvature from the seismicity distributions. For our finite-fault inversions we consider models with uniform dips from 16° to 22°, recognizing that the seismic moment varies with dip and that dip may actually vary along the megathrust.

2.2. Back-Projection Analysis

We performed a back-projection of teleseismic short-period P waves recorded in North America. This is the best station geometry (Fig. 2a) for back-projection given the location of the source region and global station distribution. The broadband P wave arrivals are very coherent and readily aligned across North America by multi-station correlation (Fig. 2b). The aligned traces were then filtered in the passband 0.5–2.0 Hz and back-projected using the procedure of XU et al. (2009) with fourth-root stacking of beam power across a constant depth target grid in the source region. Figure 2c shows the time-integrated

beam power at each grid position, demonstrating that the coherent short-period energy largely originated north of the epicenter, with two concentrations, the higher power image forming about 60 km NE of the epicenter and a second region about 50 km WNW of the epicenter. The primary bursts of coherent short-period energy are found in the first 50 s of the rupture process near the coastal region and there is little evidence for short-period bursts toward the trench (Fig. 2d). The spatial extent of the rupture indicated by these back-projections extends less than 100 km from the epicenter, which together with the 47.9 s centroid time for the gCMT inversion suggests a low overall rupture expansion velocity.

Time snapshots from the back-projection are shown in Fig. 3, capturing the irregular growth of the two lobes of short-period energy, first forming to the WNW from the epicenter in the first 20 s, then to the NE around 30 s, then with irregular northward expansion over the next 30 s. Significant coherent energy is imaged to at least 95 s lag time in the azimuth to North America. Estimates of rupture expansion velocity of 1.5–2.0 km/s can be made from the space–time pattern of these back-projection images. Similar overall behavior is found in the on-line back-projections posted by the Incorporated Research Institutions for Seismology (IRIS) (http://ds.iris.edu/spud/backprojection/10089385).

Surface wave source time functions display slight narrowing at azimuths northward from the epicenter, compatible with a low rupture velocity (1–2 km/s) along a 5° strike (http://ds.iris.edu/spud/sourcetimefunction/10090670) or about 30 s range in duration at an azimuth of 345° with a mean duration of about 105 s. Assuming unilateral rupture toward the NNW the latter measurements indicate a rupture dimension of only about 60 km and a low rupture velocity of ~1 km/s. Some component of bilateral rupture cannot be precluded, but the overall long-period source directivity is modest, similar to the short-period back-projection finiteness.

2.3. Teleseismic Finite-Fault Inversion

Guided by these constraints on the faulting geometry and rupture dimensions, several finite-fault slip inversions were performed using a least-squares
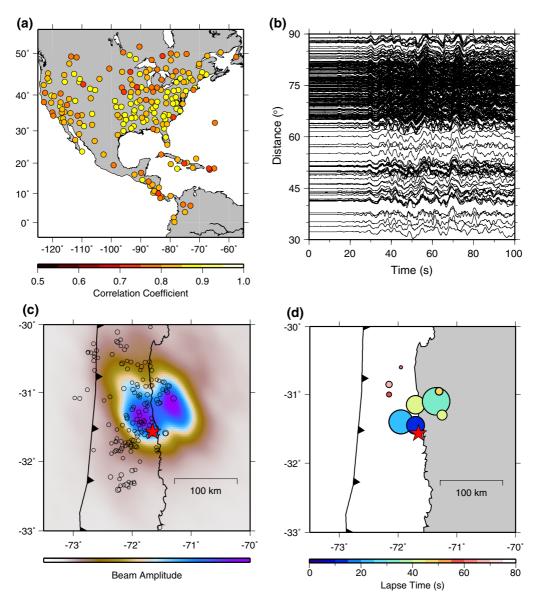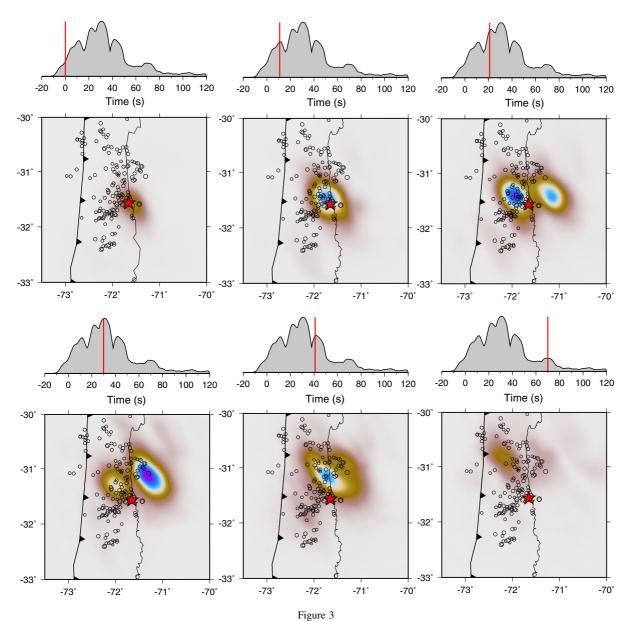
Figure 2

a Location of North American seismic stations used in the back-projection of 0.5–2.0 Hz P wave signals for the 16 September 2015 Illapel earthquake, color-coded by average correlation coefficient with all other traces. **b** The aligned, unfiltered P wave data from North America used in the back-projection. **c** Map of the time-integrated beam power distribution obtained by back-projection. The *star* indicates the USGS-NEIC epicenter, which is the reference position for aligning the first-motions of the P waves. The *small circles* are USGS-NEIC aftershock epicenters in the first 4 days following the 2015 mainshock, scaled proportional to magnitude. **d** Positions of back-projection maxima at various lapse times from the back-projection image for the North American P wave data. The relative power of peaks scales the circle radii and the points are *color-coded* by time into the rupture. An animation of the full back-projection is provided in Supplemental Movie 1

procedure applied to 135 s long recordings of 60 teleseismic broadband P waves and 42 SH waves (HARTZELL and HEATON 1983; adapted by KIKUCHI and KANAMORI 1991). In this kinematic inversion we prescribe a fault strike (5°) and dip (16° or 22°) based on slab geometry or long-period moment tensors. The fault is subdivided into 9–10 segments along-dip and 18–19 along-strike with 15×15 km subfault dimensions. The subfault source time functions are parameterized by 6 2.5 s rise time triangles offset

Figure 3

Snapshots from the North American P wave back-projection for the 2015 Illapel earthquake. Each image shows the spatial distribution of beam power at the lapse time indicated by the *red line* on the power time history shown above each map. These power peaks can be used to infer the pattern of rupture expansion with time and the associated effective rupture velocity for the portion of the 0.5- to 2.0-Hz energy that constructively interferes in the beam image. The fourth-root beam power is shown, so the image is not linearly proportional to wave amplitudes. Significant beam power is imaged for about 90 s. The *small circles* are USGS-NEIC aftershock epicenters in the first 4 days following the 2015 mainshock (*red star*), scaled proportional to magnitude. The continuous animation is provided in Supplemental Movie 1
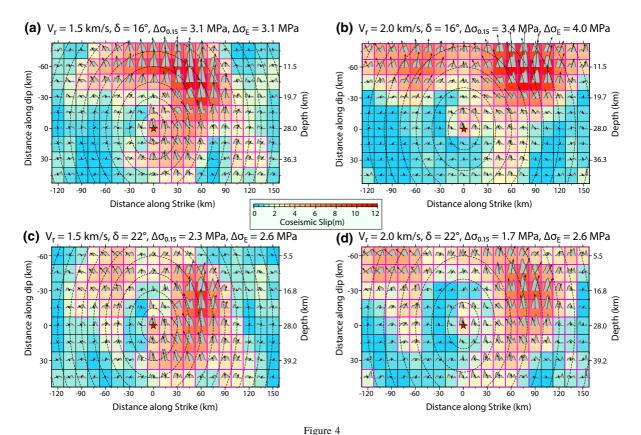
by 2.5 s, giving possible total subfault durations of 17.5 s. Rake is allowed to vary for each subfault subevent. Rupture expansion velocities of 1.5 and 2.0 km/s are considered here, although we considered a wider range of rupture velocities finding that an optimal choice is not constrained by waveform misfit,

so we imposed bounds from the back-projections and R1 time function directivity to settle on this range of possibilities. The hypocentral depth was 25 km, and Green's functions were computed for the local crustal structure from Crust 1.0 (LASKE *et al.* 2013) with addition of a 3 km deep water layer.

Four slip distributions inverted for the 16 September 2015 event are shown in Fig. 4. The solution with $V_r = 2.0$ km/s and dip 22° (Fig. 4d) is placed on the regional map in Fig. 1b, as that model is most consistent with early reports of large geodetic motions north of the hypocenter. For the shallower dip of 16°, the fault model extends further offshore, and slip occurs along the up-dip portion of the megathrust with slip centroid depths of about 16 km. For the lower rupture velocity, slip is relatively uniform and as the rupture velocity increases it splits into two patches, with more slip in the north. For the 22° dip cases the slip locates deeper on the fault closer to the coastline with slip centroid depths of 20–24 km, with two slip patches, the southern one locating further up-dip than the northern one. The

centroid times of the moment rate functions for the models vary from 50.5 to 57.3 s.

The slip models have modest rake variability, but all share an average rake of about 96°. About 80–82 % of the teleseismic P and SH waveform power is accounted for by each model, and it is not sensible to favor a particular fault parameterization based on waveform fit. Figure 5 shows an example of waveform fits for the model in Fig. 4d. The P waves are particularly well fit for all 4 models.

The along-strike distribution of large slip depends on the assumed rupture velocity and is about 180 km for $V_r = 1.5$ km/s and 240 km for $V_r = 2.0$ km/s. All of the models have a concentration of slip to the N or NW that accounts for the modest directivity seen in the R1 source time functions. All of the models also

Figure 4

Slip models for the 16 September 2015 Illapel earthquake obtained by least-squares inversion of teleseismic P and SH waves in the passband 0.005–0.9 Hz. **a** Model for $V_r = 1.5$ km/s and a dip of 16°. **b** Model for $V_r = 2.0$ km/s and a dip of 16°. **c** Model for $V_r = 1.5$ km/s and a dip of 22°. **d** Model for $V_r = 2.0$ km/s and a dip of 22°. Waveform fits are very similar for each model; those for **d** are shown in Fig. 5. Each model grid has 15 km spacing between subfaults. The *black arrows* indicate the direction and magnitude of average slip in the fault model coordinates for each subfault with the *color-scale* indicating the absolute slip magnitudes. The *red star* is the USGS-NEIC hypocentral location. The pink outline indicates the subfaults with estimated moment larger than 15 % of the peak subfault moment used for the simplified stress drop calculation, $\Delta\sigma_{0.15}$
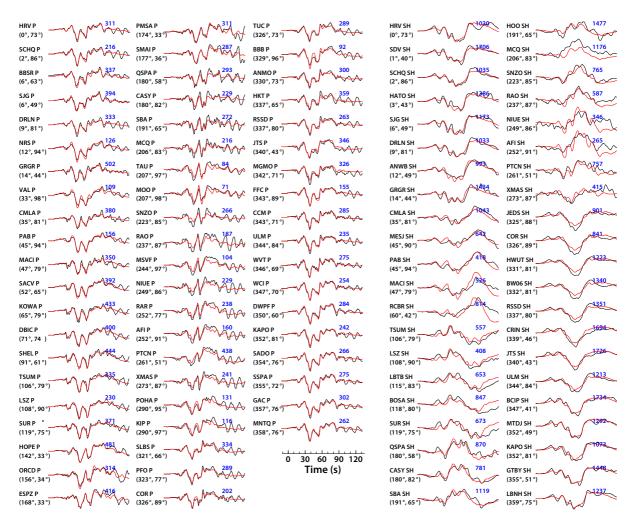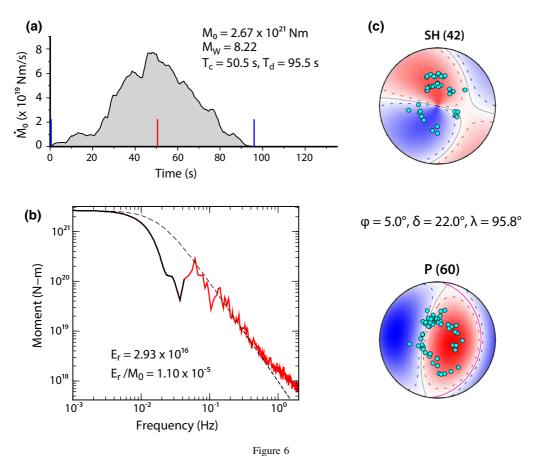
Figure 5

Observed (*black traces*) and synthetic (*red traces*) broadband P and SH ground displacements at global stations, at indicated azimuths and epicentral distances. The peak-to-peak amplitude of the data (in microns) is indicated for each trace on the *right*. The synthetics are for the finite-fault model shown in Fig. 4d

indicate a down-dip region of ∼5 m slip extending below the coastline 30–60 km north of the hypocenter.

2.4. Source Spectrum, Radiated Energy and Stress Drop Estimation

The moment rate function for the model in Fig. 4d ($V_r = 2$ km/s, dip = 22°) is shown in Fig. 6a, and there is a 95.5-s total duration, with a seismic moment of 2.67×10^{21} Nm (M_W 8.2). The centroid time is 50.5 s, several seconds larger than the gCMT centroid time, which suggests that the last 10 s of the source model may be model noise. The overall shape

of the moment rate function, which has very little dependence on the specific finite-fault inversion model, is very smooth and close to a truncated Gaussian in symmetry. This contributes to scalloping of the smooth source amplitude spectrum, with a deep notch near 0.03 Hz as shown in Fig. 6b. This source spectrum is constructed from the spectrum of the moment rate function for frequencies below 0.05 Hz and from log-averaging of far-field P wave displacement spectra corrected for radiation pattern, geometric spreading, and attenuation for frequencies above 0.05 Hz. A reference ω^{-2} spectrum with 3 MPa stress parameter and the same seismic moment is shown by the dashed line.

Figure 6

a Moment rate function for the 16 September 2015 Illapel earthquake from the teleseismic body wave finite-fault inversion in Fig. 4d. The seismic moment, M_W, centroid time T_c, and total duration, T_d estimated from this model are shown. Note the overall Gaussian shape of the source function. **b** The average source spectrum for the 2015 earthquake constructed using the moment rate function spectrum in (**a**) for frequencies below 0.05 Hz (*black line*) and log-average spectra of teleseismic P wave ground displacements corrected for geometric spreading, radiation pattern, and attenuation for frequencies above 0.05 Hz (*red line*). The total radiated energy integrated to 1 Hz, Er, and the seismic moment-scaled values are indicated. Note the deep scallop in the source spectrum near 0.03 Hz; this is a result of the smooth truncated Gaussian shape of the moment rate function. The SH and P wave radiation patterns and data sampling for the average focal mechanism from the finite-fault inversion are shown in (**c**)

The far-field radiated energy for the source was estimated from teleseismic P wave ground velocities following the basic procedure of VENKATARAMAN and KANAMORI (2004), adding relative contribution from low-frequency energy based on the moment-rate spectrum following the procedure of YE et al. (2013a). For the case shown in Fig. 6, this gives a radiated energy estimate up to 1 Hz of $E_r = 2.9 \times 10^{16}$ J, and a moment-scaled value $E_r/M_0 = 1.1 \times 10^{-5}$. The various models yield a range of radiated energy estimates because of the differences in depth of the slip distributions, spanning values from 2.2×10^{16} to 3.15×10^{16} J, with $E_r/M_0 = 0.8-1.1 \times 10^{-5}$. The broadband energy

estimate posted by IRIS is 3.2×10^{16} J (http://ds.iris.edu/spud/eqenergy/10095476) based on the method of CONVERS and NEWMAN (2011).

For the slip models in Fig. 4 we made two calculations of the stress drop. In a simplified procedure, we remove the subfaults with inverted seismic moment less than 15 % of the peak subfault seismic moment and then use the total area and average slip of the remaining subfaults (outlined in Fig. 4) in a uniform slip circular crack model, finding estimates of $\Delta\sigma_{0.15} = 1.7-3.4$ MPa. To better account for the spatially varying slip effects we also calculate the shear stress near the center of each subfault (Fig. 7 shows the result for the model in Fig. 4d) and integrate
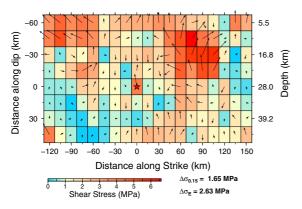
Figure 7

The distribution of stress change associated with the finite-fault slip model for the 16 September 2015 Illapel earthquake shown in Fig. 4d, where the stress values are calculated near the center of each subfault. The *black arrows* indicate the direction of the shear stress, with the color-coding indicating the value for each subfault. The slip-weighted integral of stresses is used to calculate the stress drop $\Delta\sigma_E$, whereas a simplified procedure that trims off subfaults with moments less than 15 % of the peak subfault moment and uses the remaining subfaults to estimate the rupture area and average slip for a circular stress drop estimate gives $\Delta\sigma_{0.15}$

the slip-weighted stress change to find estimates of $\Delta\sigma_E = 2.6$–4.0 MPa following the procedure of NODA et al. (2013). The corresponding estimates of radiation efficiency $\eta_r = 0.17$ (for the 16° dip models) to 0.47 (for the 22° dip model with $V_r = 2.0$ km/s) are somewhat low values due to the relatively low moment-scaled radiated energy (YE et al. 2013b).

3. Discussion and Conclusion

The teleseismic parameters estimated here are not unique, both due to the limitations of seismic wave coverage and dependence on assumed parameters such as the dip. Joint analysis of seismic, geodetic, and tsunami data will soon establish more definitive values for the rupture process. However, it is valuable to have rapidly obtained first-order seismic solutions for applications such as tsunami warning as well as for comparison with additional non-unique analyses of geodetic and tsunami data. The W-phase method applied to regional data provided a stable mechanism, seismic moment, and depth obtainable within 5–10 min after the event, which was valuable for tsunami warning. Other seismic source attributes noted here were obtained within a few hours of the event.

The models with large slip near the trench are representative of all models we found with shallower dip values. This attribute is shared by the USGS-NEIC finite-fault solution for a dip of 19° (http://earthquake.usgs.gov/earthquakes/eventpage/us20003 k7a-scientific_finitefault), and with some other on-line posted models (e.g., http://www.geol.tsukuba.ac.jp/~yagi-y/EQ/20150917/index.html). The along-strike placement of slip varies with the assumed rupture velocity, but in general such models place the slip up-dip of most aftershocks. The models with steeper dip do not extend as far off-shore, but tend to put the slip deeper on the fault as well, closer to the coast, in closer proximity to most aftershocks (Fig. 1b) and near the seaward region of short-period radiation imaged by back-projection (Fig. 2c). This is consistent with some other on-line posted models (e.g., http://www.earthobservatory.sg/news/september-16-2015-chile-earthquake). Any one-dimensional structural model does not account for the precise depth below seafloor and intersection with the trench.

The moment rate function is relatively robust for variations of rupture velocity, although the moment varies with dip. The relatively low rupture velocities of 1.5–2.0 km/s indicated by the high-frequency back-projections limit the along-strike expansion of the rupture. The lack of short-period bursts of energy from the large-slip regions near the trench indicated by the shallow dip models is similar to what has been observed for numerous large events (LAY et al. 2012). The steeper dip models do not have as strong of a discrepancy between the large-slip region and the back-projections, although the strongest feature in the back-projections is still deeper than the main slip patch. The moment-scaled radiated energy value is higher than typical of tsunami earthquakes (e.g., YE et al. 2013b) and this event does not have the distinctive long centroid time shift of a tsunami earthquake. The report of a localized 4.7 m tsunami near Coquimbo suggests concentrated slip offshore northward of the hypocenter, compatible with the steeper dipping models we considered. The overall tsunami observations do not indicate the exceptionally large tsunami expected for a near-trench tsunami earthquake.

The peak slip estimates of 8–12 m indicated by our teleseismic finite-fault inversions raise questions

about the relationship between the 2015 and 1943 Coquimbo earthquakes. While putatively rupturing in the same along-strike region of the megathrust, the estimated shallow slip for the 2015 event is as much as twice the amount of slip deficit expected to have accumulated since 1943. The 6 April 1943 rupture appears to have been smaller than the 2015 event, although it is listed as M_W 8.1 in the ISC-GEM Global Instrumental Earthquake Catalog (http://www.isc.ac.uk/iscgem/; STORCHAK *et al.* 2013). BECK *et al.* (1998) model a few P waves and estimate the seismic moment M_0 is 6×10^{20} Nm (M_W 7.9), similar to the Gutenberg-Richter $M_{S(G-R)}$ = 7.9 (ABE 1981). They obtained a simple source time function with 24 s duration from limited bandwidth data. The 1943 event produced far-field tsunami amplitudes in Japan (10–30 cm) (BECK *et al.* 1998) only about half as large as reported for 2015 (11–80 cm). There is a report of a minor local tsunami in 1943 near Los Vilos (LOMNITZ 1971). We computed an $M_{S(G-R)}$ for the 2015 event of 7.8. A reasonable interpretation is that the 2015 event rupture extended shallower or further along strike to the north on the megathrust than the 1943 event, releasing strain accumulated there over a longer interval, possibly dating back to the earlier 1880 rupture.

Rupture of up to 15 m extending up-dip close to the trench was found by YUE *et al.* (2014) for two large-slip patches in the 27 February 2010 Maule, Chile M_W 8.8 earthquake. The northern slip patch for that event was along the 1 December 1928 M_W 7.7 (ISC-GEM) rupture zone, and the large slip may have released strain accumulated possibly back to the earlier 1835 event. Shallow slip was not found for the 1 April 2014 Iquique, Chile M_W 8.1 earthquake (e.g., LAY and YUE 2014), within the great 1877 rupture zone. Thus, it is important to perform tsunami modeling to constrain the off-shore position of slip on the fault for the September 16, 2015 Chile earthquake. The rupture zone of the great 11 November 1922 earthquake to the north of the 2015 rupture, with previous large events in 1819, 1822, 1849, 1857, 1859 (BECK *et al.* 1998) is of concern for future great earthquake rupture in addition to the still un-ruptured portion of the 1877 zone in northern Chile.

REFERENCES

ABE, K. (1981), *Magnitudes of large shallow earthquakes from 1904 to 1980*, Phys. Earth Planet. Intr., *27*, 72–92.

BECK, S., S. BARRIENTOS, E. KAUSEL, and M. REYES (1998), *Source characteristics of historic earthquakes along the central Chile subduction zone*, J. South American Earth Sci., *11*, 115–129.

BRODSKY, E. E., and T. LAY (2014), *Recognizing foreshocks from the 1 April 2014 Chile earthquake*, Science, *344*, 700–702.

BROOKS, B. A., M. BEVIS, R. SMALLEY Jr., E. KENDRICK, R. MANCEDA, E. LAURÍA, R. MATURANA, and M. ARAUJO (2003), *Crustal motion in the Southern Andes (26°–36°S): Do the Andes behave like a microplate?* Geochem., Geophys., Geosys., *4*(10), 1085. doi:10.1029/2003GC000505.

CHRISTENSEN, D. H., and L. J. RUFF (1986), *Rupture process of the March 3, 1985 Chilean earthquake*, Geophys. Res. Lett., *13*, 721–724.

COMTE, D., A. EISENBERG, E. LORCA, M. PARDO, L. PONCE, R. SARAGONI, S. K. SINGH, and G. SUÁREZ (1986), *The 1985 central Chile earthquake: a repeat of previous great earthquakes in the region?* Science, *233*(4762), 449–453.

CONVERS, J. A., and A. V. NEWMAN (2011), *Global evaluation of large earthquake energy from 1997 through mid-2010*, J. Geophys. Res., *116*, B08304, doi:10.1029/2010JB007928.

DEMETS, C., GORDON, R. G., ARGUS, D. F. (2010), *Geologically current plate motions*, Geophys. J. Int., *181*, 1–80. doi:10.1111/j.1365-246X.2009.04491.x.

DUPUTEL, Z., L. RIVERA, H. KANAMORI, and G. HAYES (2012), *W phase source inversion for moderate to large earthquakes (1990–2010)*, Geophys. J. Int., *189*, 1125–1147, doi:10.1111/j.1365-246X.2012.05419.x.

DUPUTEL, Z., V. C. TSAI, L. RIVERA, and H. KANAMORI (2013), *Using centroid time-delays to characterize source durations and identify earthquakes with unique characteristics*, Earth Planet Sci. Lett., *375*, 92–100, doi:10.1016/j.epsl.2013.05.024.

GARDI, A., A. LEMOINE, R. MADARIAGA, and J. CAMPOS (2006), *Modeling of stress transfer in the Coquimbo region of central Chile*, J. Geophys. Res., *111*, B04307, doi:10.1029/2004JB003440.

HARTZELL, S. H., and T. H. HEATON (1983), *Inversion of strong ground motion and teleseismic waveform data for the fault rupture history of the 1979 Imperial Valley, California, earthquake*, Bull. Seismol. Soc. Am., *73*(6A), 1553–1583.

HAYES, G.P., and D. J. WALD (2009), *Developing framework to constrain the geometry of the seismic rupture plane in subduction zones a priori—a probabilistic approach*, Geophys. J. Int. *176*, 951–964, 2009.

HAYES, G. P., D. J. WALD, and R. L. JOHNSON (2012), *Slab1.0: A three-dimensional model of global subduction zone geometries*, J. Geophys. Res., *117*, B01302, doi:10.1029/2011JB008524.

HOLTKAMP, S. G., M. E. PRITCHARD, and R. B. LOHMAN (2011), *Earthquake swarms in South America*, Geophys. J. Int., *187*, 128–146, doi:10.1111/j.1365-246X.2011.05137.x.

KANAMORI, H., and L. RIVERA (2008), *Source inversion of W phase: speeding up seismic tsunami warning*, Geophys. J. Int., *175*, 222–238, doi:10.1111/j.1365-246X.2008.03887.x.

KELLEHER, J.A. (1972), *Rupture zones of large South American earthquakes and some predictions*. J. Geophys. Res., *77*(11), 2087–2103.

KENDRICK, E., M. BEVIS, R. SMALLEY, O. CIFUENTES, and F. GALBAN (1999), *Current rates of convergence across the Central Andes: Estimates from continuous GPS observations*, Geophys. Res. Lett., *26*, 541–544.

KENDRICK, E., M. BEVIS, R. SMALLEY Jr., and B. BROOKS (2001), *An integrated crustal velocity field for the central Andes*, Geochem. Geophys. Geosys., *2*, doi:10.1029/2001GC000191.

KHAZARADZE, G., and J. KLOTZ (2003), *Short and long-term effects of GPS measured crustal deformation rates along the South-Central Andes*, J. Geophys. Res., *108*, B4, 1–13, doi:10.1029/2002JB001879.

KIKUCHI, M., H. KANAMORI (1991), *Inversion of complex body waves—III*. Bull. Seismol. Soc. Am., *81*(6), 2335–2350.

LASKE, G., G. MASTERS., Z. MA, and M. PASYANOS (2013), Update on CRUST1.0—A 1-degree Global Model of Earth's Crust, Geophys. Res. Abstracts, *15*, Abstract EGU2013-2658, 2013.

LAY, T., H. KANAMORI, C. J. AMMON, K. D. KOPER, A. R. HUTKO, L. YE, H. YUE, and T. M. RUSHING (2012), *Depth-varying rupture properties of subduction zone megathrust faults*, J. Geophys. Res., *117*, B04311, doi:10.1029/2011JB009133.

LAY, T., YUE, H., E. E. BRODSKY, and C. AN (2014), *The 1 April 2014 Iquique, Chile Mw 8.1 earthquake rupture sequence*, Geophys. Res. Lett., *41*, doi:10.1002/2014GL060238.

LOMNITZ, C. (1971). *Grandes terremotos y tsunamis en Chile durante el período 1535–1955*, Geofisica Panamericana, *1*(1), 151–178.

MÉTOIS, M., A. SOCQUET, and C. VIGNY (2012), *Interseismic coupling, segmentation and mechanical behavior of the central Chile subduction zone*, J. Geophys. Res., *117*, B03406, doi:10.1029/2011JB008736.

MORENO, M., M. ROSENAU, and O. ONCKEN (2010), *2010 Maule earthquake slip correlates with pre-seismic locking of Andean subduction zone*, Nature, *467*, 198–202, doi:10.1038/nature09349.

NISHENKO, S. P. (1985), *Seismic potential for large and great interplate earthquakes along the Chilean and southern Peruvian margins of South America: a quantitative reappraisal*, J. Geophys. Res., *90*, 3589–3615.

NODA, H., N. LAPUSTA, and H. KANAMORI (2013), *Comparison of average stress drop measures for ruptures with heterogeneous stress change and implications for earthquake physics*, Geophys. J. Int., *193*, 1691–1712, doi:10.1093/gji/ggt074.

NORABUENA, E., L. LEFFLER-GRIFFIN, A. MAO, T. DIXON, S. STEIN, S. I. SACKS, L. OCOLA, and M. ELLIS (1998), *Space geodetic observations of Nazca–South America convergence across the central Andes*, Science, *270*, 358–362.

STORCHAK, D.A., D. DI GIACOMO, I. BONDÁR, E. R. ENGDAHL, J. HARRIS, W. H. K. LEE, A. VILLASEÑOR, and P. BORMANN (2013). *Public release of the ISC-GEM global instrumental earthquake catalogue (1900–2009)*, Seism. Res. Lett., *84*(5), 810–815, doi:10.1785/0220130034.

VENKATARAMAN, A., and H. KANAMORI (2004), *Observational constraints on the fracture energy of subduction zone earthquakes*, J. Geophys. Res., *109*, B05302, doi:10.1029/2003JB002549.

VIGNY, C., A. RUDLOFF, J.-C. RUEGG, R. MADARIAGA, J. CAMPOS, and M. ALVAREZ (2009), *Upper plate deformation measured by GPS in the Coquimbo gap, Chile*, Phys. Earth Planet. Inter., *175*(1–2), 86–95.

XU, Y., K. D. KOPER, O. SUFRI, L. ZHU, A. R. HUTKO (2009), *Rupture imaging of the M_W 7.9 12 May 2008 Wenchuan earthquake from back projection of teleseismic P waves*, Geochem. Geophys. Geosyst., *10*, Q04006, *doi:*10.1029/2008GC002335.

YE, L., T. LAY, H. KANAMORI, and K. D. KOPER (2013a), *Energy release of the 2013 M_W 8.3 Sea of Okhotsk earthquake and deep slab stress heterogeneity*, Science, *341*, 1380–1383, doi:10.1126/science.1242032.

YE, L., T. LAY, and H. KANAMORI (2013b), *Large earthquake rupture process variations on the Middle America megathrust*, Earth Planet. Sci. Lett., *381*, 147–155, doi:10.1016/j.epsl.2013.08.042.

YUE, H., T. LAY, L. RIVERA, C. AN, C. VIGNY, X. TONG, and J. C. BÁEZ SOTO (2014), *Localized fault slip to the trench in the 2010 Maule, Chile M_w 8.8 earthquake from joint inversion of high-rate GPS, teleseismic body waves, InSAR, campaign GPS, and tsunami observations*, J. Geophys. Res., *119*, 7786–7804, doi:10.1002/2014JB011340.